A laboratory-scale numerical study of the effects of bank-attached vane submergence on flow pattern and bed shear stress distribution

Bahrami-Yarahmadi, Mohammad; Erick, Roya; Shafai-Bejestan, Mahmood; Mosselman, Erik

DOI
10.1080/00221686.2024.2446582

Publication date
2025

Document Version
Final published version

Published in
Journal of Hydraulic Research

Citation (APA)
Bahrami-Yarahmadi, M., Erick, R., Shafai-Bejestan, M., & Mosselman, E. (2025). A laboratory-scale numerical study of the effects of bank-attached vane submergence on flow pattern and bed shear stress distribution. *Journal of Hydraulic Research*, *63*(1), 15-31. https://doi.org/10.1080/00221686.2024.2446582

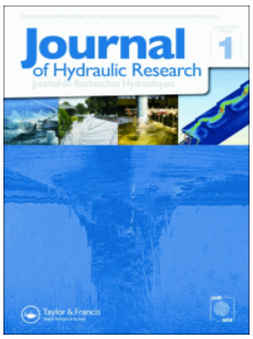

Journal of Hydraulic Research

ISSN: (Print) (Online) Journal homepage: www.tandfonline.com/journals/tjhr20

A laboratory-scale numerical study of the effects of bank-attached vane submergence on flow pattern and bed shear stress distribution

Mohammad Bahrami-Yarahmadi, Roya Erick, Mahmood Shafai-Bejestan & Erik Mosselman

To cite this article: Mohammad Bahrami-Yarahmadi, Roya Erick, Mahmood Shafai-Bejestan & Erik Mosselman (2025) A laboratory-scale numerical study of the effects of bank-attached vane submergence on flow pattern and bed shear stress distribution, Journal of Hydraulic Research, 63:1, 15-31, DOI: 10.1080/00221686.2024.2446582

To link to this article: https://doi.org/10.1080/00221686.2024.2446582

Published online: 03 Feb 2025.

JOURNAL OF HYDRAULIC RESEARCH
2025, VOL. 63, NO. 1, 15–31
https://doi.org/10.1080/00221686.2024.2446582

IAHR AIRH International Association for Hydro-Environment Engineering and Research
Hosted by Spain Water and IWHR, China
Taylor & Francis Taylor & Francis Group

RESEARCH PAPER

A laboratory-scale numerical study of the effects of bank-attached vane submergence on flow pattern and bed shear stress distribution

Mohammad Bahrami-Yarahmadi[a], Roya Erick[a], Mahmood Shafai-Bejestan[a] and Erik Mosselman[b,c]

[a]Department of Water Structures, Faculty of Water and Environmental Engineering, Shahid Chamran University of Ahvaz, Ahvaz, Iran; [b]Faculty of Civil Engineering and Geosciences, Delft University of Technology, Delft, the Netherlands; [c]Deltares, Delft, the Netherlands

ABSTRACT

Bank-attached vanes (BAVs) are triangular vanes to protect the outer banks of river bends against erosion. However, their performance for higher or lower bankfull depth is uncertain. This study aims to validate the Flow3D numerical model, to study the effects of submergence and emergence of BAVs on flow patterns and bed shear stresses at $h/H = 0.5$, 1, 1.5 and 2 (h = flow depth, H = BAV height) and constant Froude number. The results showed that a recirculation cell, 1.046 times the structure's length, developed behind the emerged BAV ($h/H = 0.5$), whereas no recirculation occurred behind the submerged BAV ($h/H = 1$, 1.5 and 2). Increasing the flow depth undermined the BAV's effectiveness in reducing bed shear stress near the outer bank. The bed shear stress near the BAV's tip at $h/H = 0.5$, 1, 1.5 and 2 was equivalent to 1.67, 1.45, 1.3 and 1.24 times the average bed shear stress upstream of the bend, respectively.

ARTICLE HISTORY
Received 6 October 2023
Accepted 18 December 2024
Open for discussion

KEYWORDS
Flow3d; flow depth; FLOW pattern; hydraulic

1. Introduction

Riverbank erosion is a key problem in river engineering. It can destroy buildings, infrastructure and agricultural lands, but also threatens aquatic ecosystems (Biedenharn et al., 1997; Salehzadeh et al., 2023). Two essentially different approaches to counter this erosion can be distinguished. The first approach focuses on increasing the resistance against erosion by reinforcing the bank, e.g. by revetment of the slope or scour protection at the bank toe. The second approach reduces the erosive attack on the riverbank (Bora & Kalita, 2021), following two possible principles. The first principle is that the countermeasure keeps the main flow away from the bank (groynes, spurs, stream barbs). The second principle is based on counteracting the transverse helical flow that is generated in river bends by an interaction between centrifugal forces and transverse pressure gradients. This helical flow causes deeper toe scour and higher flow velocities at the outer bank (Blanckaert & Graf, 2001; Deng et al., 2019; Julien, 2002; Kashyap et al., 2012; Koken & Gogus, 2015; Khosronejad, Kozarek, Diplas et al., 2015; Pandey et al., 2018). The counteracting of helical flow can be achieved by structures that generate a vortex rotating in the opposite direction (submerged vanes, bandal-like structures), cf. Odgaard (2009). A disadvantage of structures like groynes and spurs is that they produce deep scour at the nose (Oberhagemann et al., 2020) that could lead to the collapse of the structure or even induce flow slides of the riverbank (Mastbergen et al., 2019; Van der Wal, 2020). The scour can be reduced by designing the groyne or the spur in such a way that water can pass, with decreasing blockage from the root in the bank to the nose of the structure. This design reduces the transverse gradients in flow velocity and thereby the associated turbulence. Van der Wal's (2020) permeable groynes form an example.

Innovations have resulted in novel structures that combine different working principles. For instance, Rodríguez-Amaya et al. (2020) applied submerged vanes in groyne-like arrangements that not only reduce the effects of helical flow but also keep the main flow away from the bank. Bank-attached vanes (BAVs) combine three working principles. First, they keep the main flow away from the outer bank by protruding into the river. Second, they generate a vortex counteracting the adverse transverse helical flow thanks to their placement under an angle with respect to the bank. Third, they reduce local scouring around the nose because they have a triangular shape that slopes from the highest level at the bank (maximum blockage) to zero elevation at the nose (zero blockage). The height of the vane at the bank is equal to the flow depth at bankfull discharge. The BAV is installed at a slight angle ($\alpha = 20$–$30°$) to the upstream bank (Bahrami Yarahmadi & Shafai Bejestan, 2016a; Galia et al., 2016; NRCS, 2007; Pagliara & Kurdistani, 2017; Rosgen, 2006; Shields, 1983). The BAV, unlike a conventional spur dike, only slightly

CONTACT Mohammad Bahrami-Yarahmadi m.bahrami@scu.ac.ir

disturbs the river flow and is suitable for the protection of outer banks of river bends against erosion as well as aquatic habitat improvement (Hey, 1996; Rosgen, 1996, 2006). Similar to all in-stream structures, BAVs still produce local scour at their tip which may cause their failure. Bahrami Yarahmadi and Shafai Bejestan (2016b) found that the scour depth around the nose of a BAV is about 49% less than around an emerged spur dike. Bahrami-Yarahmadi et al. (2020a) found that the maximum scour depth and volume at a series of BAVs are 44% and 70% lower than at rectangular spur dikes.

Bhuiyan et al. (2010) carried out the first systematic study of the performance of BAVs in a sinusoidal sand-bed bend channel. BAVs were shown to fill the erosion hole formed at the outer bank with sediments, pushing the thalweg toward the centre of the channel. BAVs installed in series at 30° were found to outperform 20° BAVs. Bahrami-Yarahmadi (2014) and Bahrami Yarahmadi and Shafai Bejestan (2016a) studied how BAVs affected scour and deposition in a 90° bend under clear-water conditions. They found that the lowest scour depth occurred at the toe of BAVs if their spacing was five times the vane's effective length (or less), their angle with the upstream bank was 23 or 30°, and their effective length was one-fifth of the flume width. Bahrami Yarahmadi and Shafai Bejestan (2020b) experimentally studied secondary flows and bed shear stress around a single BAV. They found that a vane-induced secondary flow developed opposite to and stronger than the bend-induced secondary flow behind the vane. This reduced bed shear stress near the outer bank by 80%, prevented the bend-induced secondary flow from reaching the outer bank, and transported the bed sediment transversely toward the outer bank creating a longitudinal bar. Researchers have used this vane advantage and studied new structures to increase sedimentation capacity near the outer bank. Ferro et al. (2019) studied the combination of a triangular vane with a permeable spur dike. Shokrian Hajibehzad et al. (2020) investigated the performance of triangular vanes attached to permeable groynes in series and confirmed the results of Ferro et al. (2019). Kalamizadeh et al. (2021) studied the effects of permeable BAVs made by six-pillar concrete elements on the scour and deposition pattern in a 180° bend.

We present the first numerical analysis of the effects of BAVs, but research on other in-stream structures to protect river banks can put this into perspective. For instance, Khosronejad, Hill et al. (2013), Khosronejad, Kozarek, and Sotiropoulos et al. (2014), Khosronejad, Diplas et al. (2016), Khosronejad, Kozarek, Diplas et al. (2018) and Kang et al. (2020a, 2020b) carried out elaborate laboratory experiments and numerical simulations of flow structure and scour around rock vanes, cross vanes, J-hook vanes, bendway weirs, and w-weirs.

Despite earlier research, the effect of submergence and emergence on flow patterns and bed shear stress around BAVs has not received attention. This is relevant for choosing the representative conditions for design. The studies of Jalili et al. (2018) on a series of bandal-like spur dikes and Safaripour et al. (2022) on a submerged vane showed that the submergence ratio affects the bed topography around the structures. Present design criteria indicate that the height of the BAV at the outer bank should be equal to the flow depth at bankfull discharge. However, in many natural rivers, flow discharge and flow depth vary over time and this affects flow patterns and bed shear stress. The objective of this study is therefore to numerically assess the effects of submergence and emergence of BAVs on flow patterns and bed shear stresses. For this we use the Flow3D software, validating the results against measured data from laboratory experiments.

2. Materials and methods

2.1. Experimental model

We used the experimental data of Bahrami-Yarahmadi et al. (2020b) to validate the Flow3D numerical model. The experiments were conducted in a 70-cm wide curved flume (90° mild bend, $R/B = 4$, where R denotes the average bend radius, and B is the flume width). The straight reaches upstream and downstream of the 90° bend were 5 and 3 m long, respectively. The inner and outer radii of the flume bend were 2.45 and 3.15 m. Flume walls were made of glass in straight reaches upstream and downstream of the bend, whereas 10-mm Plexiglas walls were used in the curved part. The slide gate at the end of the downstream straight reach regulates the flow depth. The flume bed consisted of uniform sediment with $d_{50} = 1.5$ mm and a geometric standard deviation, σ_g, of 1.2 ($\sigma_g = \sqrt{d_{84}/d_{16}}$), where d_{16} and d_{84} are the grain sizes for which 16% and 84% of sampled particles are finer, respectively) (Bahrami-Yarahmadi et al., 2020b).

Bahrami-Yarahmadi et al. (2020b) carried out experiments with and without the BAV. In both groups of experiments, three-dimensional components of the flow velocity were measured by an ACM3-RS JFE ALEC electro-magnetic velocity meter with a $\pm 2\%$ or 0.5 cm s^{-1} accuracy. In both cases, the bed sediments were levelled and stabilized so that no sediment particle would move along the flume during velocity measurements. The flow depth was considered equal to the height of the BAV. In both experiments, the discharge and flow depth (in the straight reach upstream of the bend) were 22 l s^{-1} and 13 cm. Accordingly, the Froude (F_r) and Reynolds (R_e) numbers of the flow in the straight reach upstream of the bend were 0.214 and 22799, respectively.

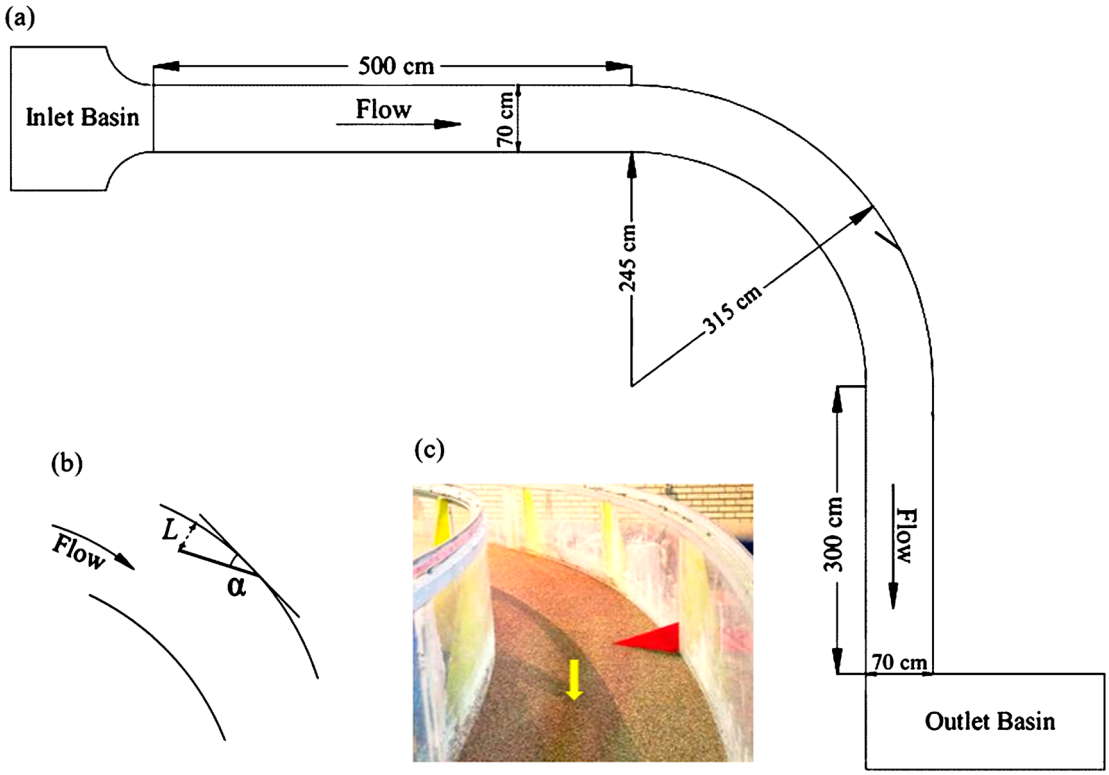

Figure 1. (a) Plan view of the flume and the triangular vane layout in the outer bank, (b) sketch of the vane parameters, (c) photograph of the triangular vane in the bend.

A single BAV was used in experiments with the vane. The BAV was made of 5-mm Plexiglas and installed at the outer bend at a position of 72° relative to the beginning of the bend with a 30° angle (α). The height, the length (L_v), and the effective length (L) (i.e. distance of the tip of the vane in the bed from the outer bank) of the BAV were 13, 30 and 14 cm, respectively. Figure 1 shows the experimental flume plan and the BAV layout.

2.2. Numerical modelling

Flow3D can simulate an extensive range of flow conditions for complex fluid dynamics problems. The software package relies on the finite-volume method (FVM) to solve the equations governing the flow by structured meshing and uses the volume of fluid (VOF) method to calculate the free water surface in open channels. The model can analyse the flow field in one, two and three dimensions (Fathi-Moghaddam et al., 2018; Parsaie et al., 2022).

Governing equations

This study employed the Flow3D software to solve the 3D equations governing the movement of flow. The researchers utilized the continuity and momentum equations as the fundamental governing equations in their analysis. The continuity equation in its incompressible form is represented by Equation (1):

$$V_F\frac{\partial(\rho)}{\partial t}+\frac{\partial}{\partial x}(uA_x)+\frac{\partial}{\partial y}(vA_y)+\frac{\partial}{\partial z}(wA_z)=\frac{R_{SOR}}{\rho} \tag{1}$$

where (u, v, w) denote the velocity components in the (x, y, z) directions, (A_x, A_y, A_z) represent the fractional area of flow in the (x, y, z) directions, V_f represents the fractional volume of flow, ρ denotes the mass density of the fluid, and R_{SOR} represents the mass source (Fathi-Moghaddam et al., 2018). The momentum equations can be expressed as follows:

$$\frac{\partial u}{\partial t}+\frac{1}{V_F}\left(uA_x\frac{\partial u}{\partial x}+vA_y\frac{\partial u}{\partial y}+wA_z\frac{\partial u}{\partial z}\right)=-\frac{1}{\rho}\frac{\partial p}{\partial x}+Gx+fx \tag{2}$$

$$\frac{\partial v}{\partial t}+\frac{1}{V_F}\left(uA_x\frac{\partial v}{\partial x}+vA_y\frac{\partial v}{\partial y}+wA_z\frac{\partial v}{\partial z}\right)=-\frac{1}{\rho}\frac{\partial p}{\partial y}+Gy+fy \tag{3}$$

$$\frac{\partial w}{\partial t}+\frac{1}{V_F}\left(uA_x\frac{\partial w}{\partial x}+vA_y\frac{\partial w}{\partial y}+wA_z\frac{\partial w}{\partial z}\right)=-\frac{1}{\rho}\frac{\partial p}{\partial z}+Gz+fz \tag{4}$$

In which (G_x, G_y, G_z) represent the body accelerations, while (f_x, f_y, f_z) represent the accelerations caused by viscosity in different directions (Fathi-Moghaddam et al., 2018).

Turbulence models

We employed the k-ε standard, RNG and LES turbulence closure models to validate the numerical model. In the simulations of the present study, we found that results from the RNG turbulence model agreed best with the laboratory data (see the Validation section below). The RNG turbulence model is based on the Re-Normalisation Group (RNG) and employs a statistical approach to solve the averaged equations for turbulence quantities, specifically turbulence kinetic energy (k) and turbulence dissipation rate (ε). This model is widely used in turbulent flow simulations due to its effectiveness in capturing complex turbulent behaviour. The turbulent flow simulation using the RNG turbulence model involves solving the following equations:

$$\frac{\partial}{\partial t}(\rho k) + \frac{\partial}{\partial x_i}(\rho k u_i) = \frac{\partial}{\partial x_j}\left[\left(\mu + \frac{\mu_t}{\sigma_k}\right)\frac{\partial k}{\partial x_j}\right] + P_k - \rho\varepsilon \quad (5)$$

$$\frac{\partial}{\partial t}(\rho \varepsilon) + \frac{\partial}{\partial x_i}(\rho \varepsilon u_i) = \frac{\partial}{\partial x_j}\left[\left(\mu + \frac{\mu_t}{\sigma_\varepsilon}\right)\frac{\partial \varepsilon}{\partial x_j}\right] + C_{1\varepsilon}\frac{\varepsilon}{k}P_k - C^*_{2\varepsilon}\rho\frac{\varepsilon^2}{k} \quad (6)$$

where $C^*_{2\varepsilon} = C_{2\varepsilon} + \frac{C_\mu \eta^3(1-\eta/\eta_0)}{1+\beta\eta^3}$, $\eta = Sk/\varepsilon$, $S = \sqrt{2S_{ij}S_{ij}}$ and $S_{ij} = \frac{1}{2}\left(\frac{\partial u_i}{\partial x_j} + \frac{\partial u_j}{\partial x_i}\right)$.

in which u_i signifies the velocities in the x, y and z directions, t denotes time, ρ denotes the volume-fraction averaged mass density, μ_t denotes turbulent viscosity, and μ denotes molecular viscosity. Below are the values of the constants in the above equations (Yakhot et al., 1992):

$$C_\mu = 0.0845,\ C_{1\varepsilon} = 1.42,\ C_{2\varepsilon} = 1.68,\ \sigma_k = 0.7194,$$
$$\sigma_\varepsilon = 0.7194,\ \eta_0 = 4.38,\ \beta = 0.012$$

Computational domain, boundary conditions, and grid layout

After representing the 90° curved flume in Flow3D, the computational domain was meshed using four mesh blocks (Figure 2). Mesh block #1 was used for the straight reach upstream of the bend, mesh block #2 for the flume bend, mesh block #3 for the straight reach downstream of the bend, and mesh block #4 for the area surrounding the BAV. Three simulations were conducted to determine the optimal mesh size. In the first simulation, the mesh blocks 1–4 had 2, 1, 1 and 0.4 cm cells, respectively. The cell sizes were changed to 2, 1.5, 1.5 and 0.4 cm in the second simulation and 3, 2, 3 and 0.4 cm in the third run. Given the 0.5 cm thickness of the BAV, 0.4 cm cells were always used in mesh block #4. The total number of cells in the first, second and third simulations were 3882420, 1444510 and 782625, respectively. Figure 3 shows the simulation results. The horizontal and vertical axes represent the cell count in the simulation and the depth-averaged longitudinal velocity at 72° and 76° sections. As shown, using more than 1444510 cells does not change the depth-averaged longitudinal velocity significantly. Increasing the number of cells does not make the results more accurate but increases the simulation runtime. Therefore, we used a total of 1444510 cells. Mesh blocks #1 to #4 comprised 52500, 890420, 130340 and 371250 cells, respectively.

The conditions at the upstream and downstream boundaries and the initial conditions are shown in Figure 4. A volume flow rate was imposed at the inlet of the mesh block upstream of the bend and a pressure at the outlet of the mesh block downstream of the bend. A wall condition was imposed at the flume walls and the bed, and a symmetry condition at interfaces between mesh blocks and the free surface of the fluid. In all simulations, the length of the straight reach upstream of the bend was considered equal to 5 m so that the flow is fully developed before entering the bend and its excess turbulence is depleted.

The simulations were terminated when the discharge stabilized to a constant level along the entire flume, i.e. the discharges into and out of the flume were balanced. The discharge stabilized along the flume within 170–190 s in different simulations. Accordingly, a fixed runtime of 200 s was selected for all simulations.

Boundary layer mesh

The y^+ value determines the behaviour of the wall function for flow near the walls. This parameter should have a value between around 30 and 300 when using the standard formula for the wall function. Its definition reads:

$$y^+ = \frac{u_* y_s}{\nu} \quad (7)$$

where u_* is the shear velocity, y_s is the distance from the wall to the centre of the first cell, and ν is the kinematic viscosity of the fluid (Rodi, 2017). The size of the mesh cells was chosen in such a way that the y^+ value falls within the above-mentioned range.

Research goals and scenarios

This study investigates the flow patterns and the bed shear stress around a single BAV (for different submergence levels) in a 90° mild bend. A single BAV was installed at the 72° section of the bend at a 30° angle with the upstream bank. The BAV length and height were 21 and 13 cm, respectively, in all runs. The discharge and flow depth were chosen in such a way that the F_r in all simulations was equal to 0.214. Table 1 lists the specifications of the simulation runs.

Validation

The numerical model validation aimed to select the best turbulence model to simulate the flow velocity and pattern more accurately. LES, RNG and k–ε turbulence

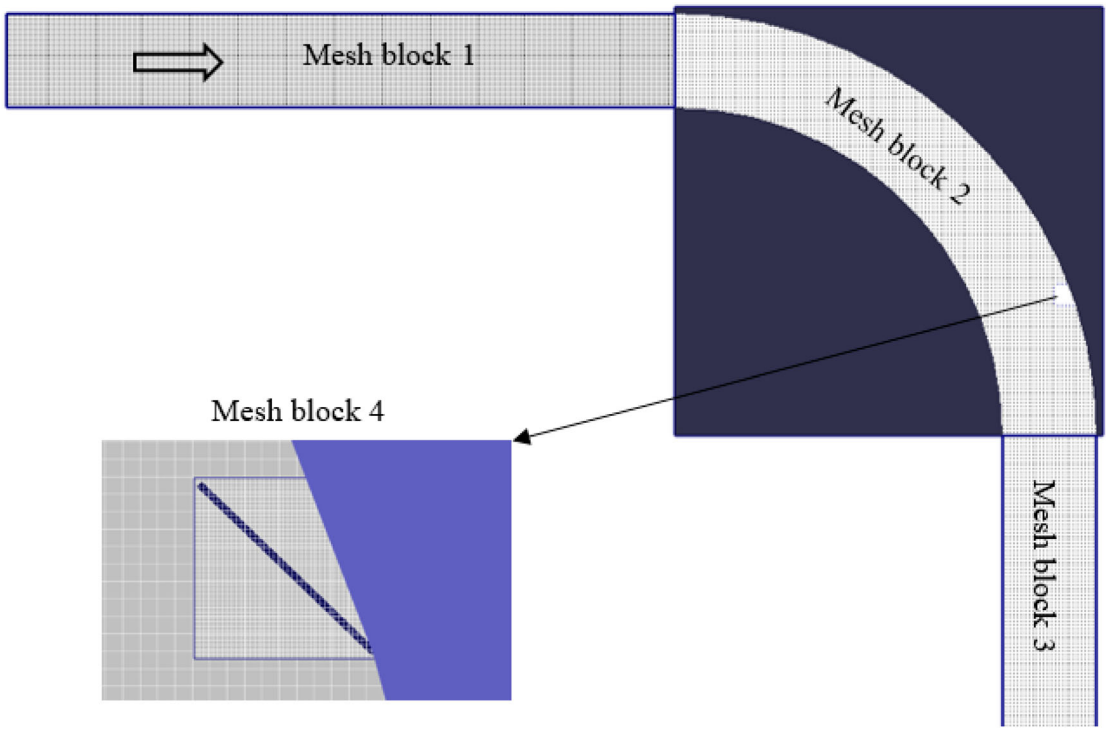

Figure 2. Plan view of the mesh blocks.

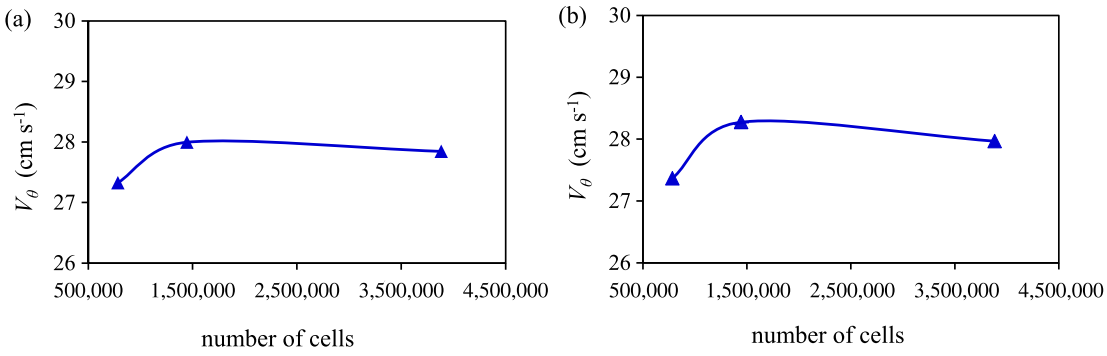

Figure 3. Mesh independence: (a) the 72° section, 30 cm from the outer bank, (b) the 76° section, 30 cm from the outer bank.

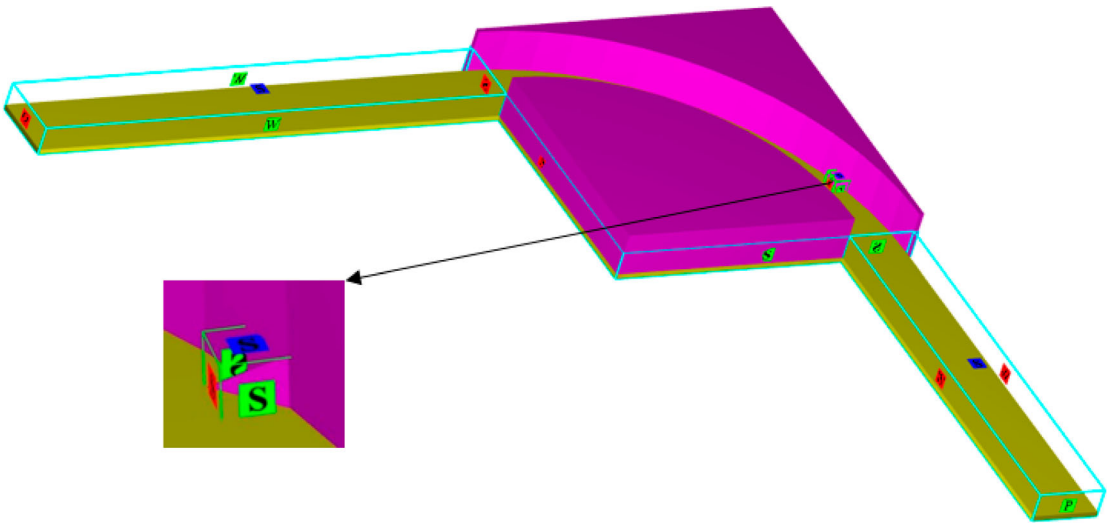

Figure 4. Computational domain and applied boundary conditions.

Table 1. Simulation runs.

Test name	α (°)	Q (l s^{-1})	h (cm)	Number of cells
With BAV	30	7.77	6.50	1,196,636
With BAV	30	22.00	13.00	1,365,210
With BAV	30	40.40	19.50	1,625,334
With BAV	30	62.20	26.00	1,923,286
Without BAV	–	7.77	6.50	1,098,356
Without BAV	–	22.00	13.00	1,289,610
Without BAV	–	40.40	19.50	1,489,614
Without BAV	–	62.20	26.00	1,738,786

Note: α = BAV angle with the upstream bank, Q = flow discharge, h = flow depth.

models employed and evaluated in previous studies were used to validate the numerical model.

Figure 5 compares the longitudinal velocity of the experimental model, as explained in Section 2.1, with those obtained from LES, RNG and k–ε turbulence models. Here 0 and 70 on the horizontal axis represent the inner and outer bend walls. Figure 5 reveals similar results for all turbulence models that are also qualitatively consistent with the experimental data. We evaluated the turbulence models based on percent bias (PBIAS):

$$\text{PBIAS} = \left(\frac{\sum_{i=1}^{n} S_i - \sum_{i=1}^{n} O_i}{\sum_{i=1}^{n} O_i} \right) \times 100 \qquad (8)$$

where n denotes the number of data points, O_i is the observed velocities, and S_i is the simulated velocities from Flow3D. PBIAS shows the average tendency of the simulated data to be lower or larger than experimental results (Gupta et al., 2001; Shampa et al., 2020). The acceptable PBIAS ranges from 0 to 25% ($0 \leq \text{PBIAS} \leq 25\%$) (Bracmort et al., 2006; Santhi et al., 2002; Shampa et al., 2020). PBIAS values of −11, −11.8 and −11.9% were calculated for simulations of the transverse profile of the longitudinal velocity at the 72° section, 6 cm above the bed, using RNG, k–ε and LES models, respectively. Differences between the results of turbulence models and experimental data can be attributed to the errors of measurement instruments (flow and velocity meters), modelling errors, errors in the VOF and fractional area-volume obstacle representation (FAVOR) methods, truncation errors, convergence errors, round-off errors, mathematical modelling errors, errors caused by turbulence models.

Figure 6 illustrates the flow patterns resulting from experimental data and three turbulence models (RNG, k–ε and LES) at the 76° cross-section. Again 0 and 70 on the horizontal axis represent the inner and outer bend walls. The experimental results in Figure 6a suggest a vortex near the outer bank under the influence of the BAV, which rotates opposite to the bend-induced secondary flow (Bahrami-Yarahmadi et al., 2020b). According to Figure 6, LES does not simulate structure- and bend-induced vortices and their boundaries well enough, whereas the results of RNG and k–ε are closer to the experiments.

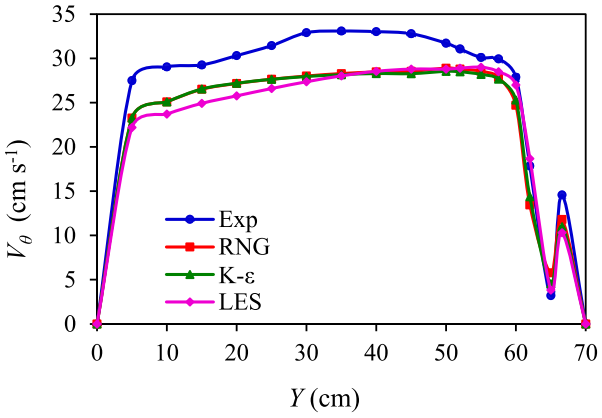

Figure 5. The transverse profile of longitudinal velocity at the 72° cross-section, 6 cm above the bed.

Based on the PBIAS scores of the three turbulence models and Figure 6, we selected the RNG turbulence model for the simulations.

3. Results and discussion

3.1. Flow pattern in simulations with BAV

Figure 7 depicts the flow pattern and longitudinal velocity contour at different cross-sections for the simulation with h = 13 cm, where 0 on the horizontal axis represents the inner bend wall, and 70 represents the outer bend wall. A vortex is formed at the 70° cross-section (on the right of the vane) near the outer bank, rotating opposite to the bend-induced vortex. The vortex results from the flow passing over the BAV, strikes the flume bed, and prevents the bend-induced vortex from reaching the outer bank. The vane-induced vortex becomes larger at the 72° cross-section (where the vane is installed) than the same vortex at the 70° section. Further away from the vane and toward the end of the bend, the vortex core moves away from the outer bank while approaching the water surface. The core is 3 cm below the water surface at the end of the bend (90° cross-section). The vane-induced vortex is larger downstream of the bend than inside. For example, the vane-induced vortex measures 14 and 22 cm ($0.67L_v$ and $1.04L_v$) at the 74° section and 2 m downstream the bend, respectively. Figure 7 shows the bend- and vane-induced vortices to continue up to 4 m downstream of the bend.

Another observation in Figure 7 is that the BAV at the outer bend reduces the flow velocity near the outer bank, albeit over a limited distance. The flow velocity near the outer bank at the 90° section is higher than at its upstream sections.

The scour and sedimentation pattern around flow-altering structures is affected by the flow pattern around these structures. Factors such as the structure's shape, length, orientation, height, position in the bend, and hydraulic parameters (e.g. h and $\mathsf{F_r}$) influence the

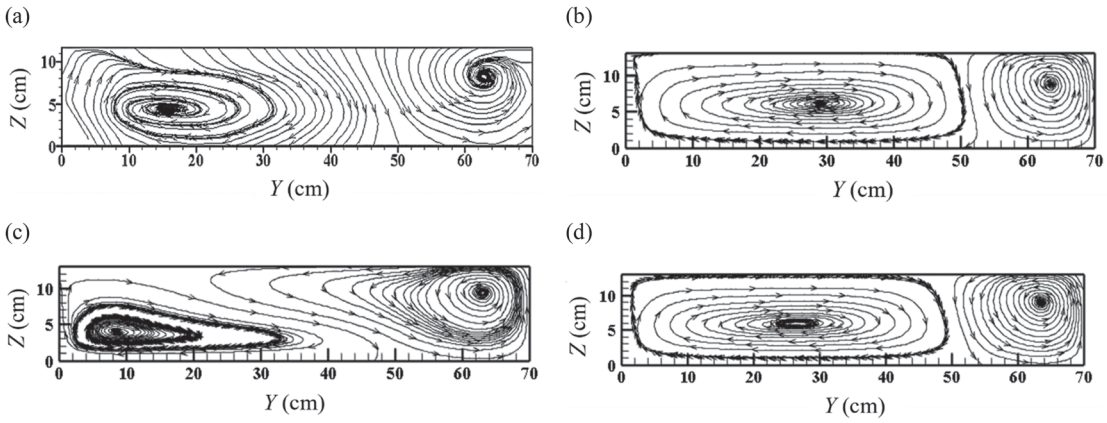

Figure 6. Flow pattern at the 76° cross-section according to the (a) Experimental model, (b) RNG model, (c) LES model, (d) k–ε model.

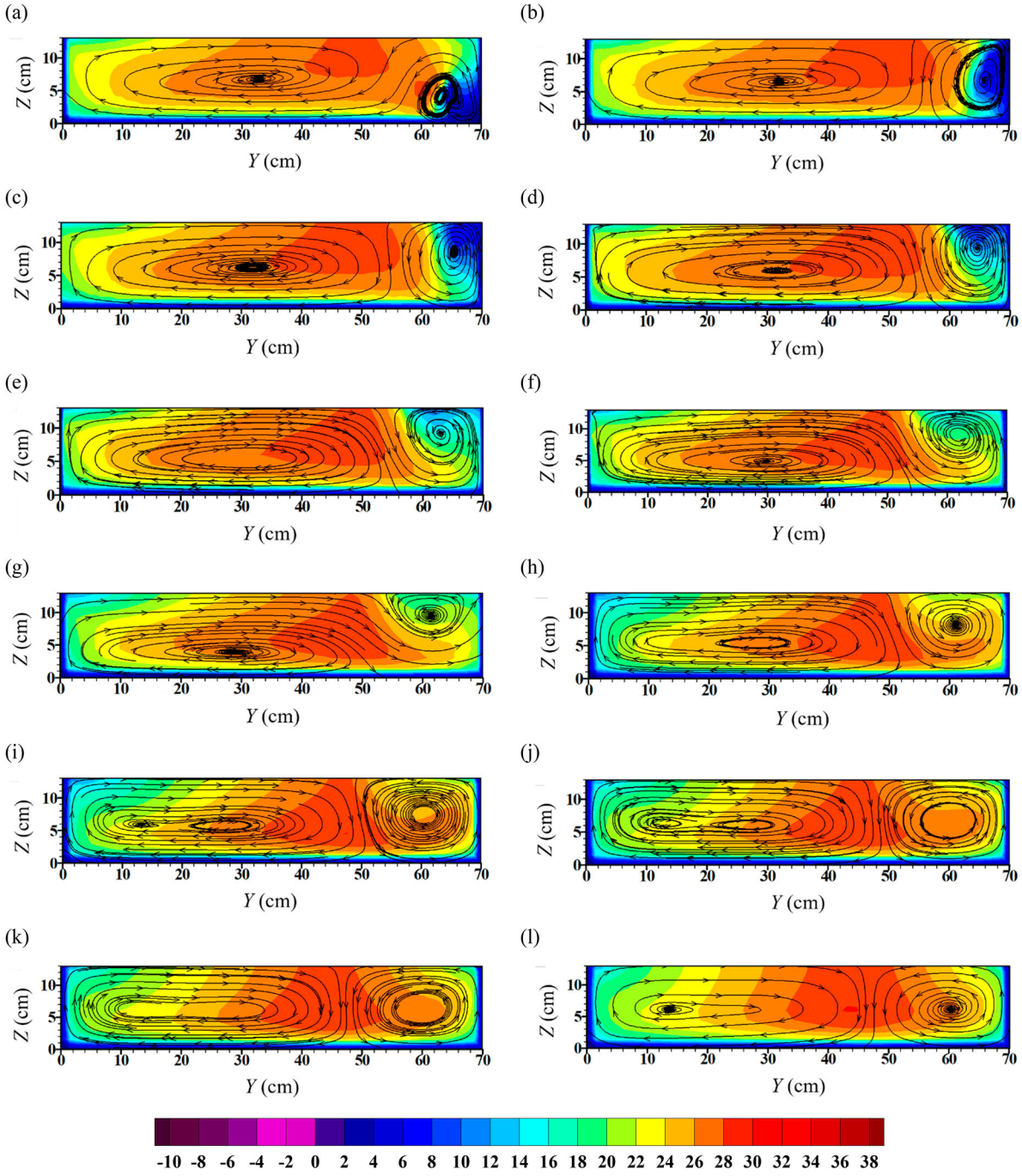

Figure 7. Flow pattern and longitudinal velocity contour (cm s^{-1}) for the simulation with 1*H* flow depth at sections: (a) 70°, (b) 72°, (c) 74°, (d) 76°, (e) 80°, (f) 85°, (g) 90°, (h) 0.5 m downstream the bend, (i) 1 m downstream the bend, (j) 2 m downstream the bend, (k) 3 m downstream the bend, (l) 4 m downstream the bend.

surrounding flow patterns. Accordingly, flow patterns emerging around BAVs differ from those around other in-stream structures. Zhang et al. (2009) found a near-bank vertical vortex with a horizontal axis upstream of an emerged impermeable rectangular spur dike (installed at 90° in a straight channel). In contrast, two counter-rotating vortices formed downstream of the spur dike near the bank. Zhang et al. also reported a small, clockwise, horizontal vortex with a vertical axis at the water surface upstream of the spur dike. A large clockwise horizontal vortex with a vertical axis also formed at the water surface downstream of the spur dike. Bahrami-Yarahmadi et al. (2020a) observed that a horizontal vortex was formed at the bed and the water surface downstream of an emerged rectangular spur dike. Jia et al. (2005) showed that the bend-induced secondary flow behind a submerged weir (installed with an angle of 20° to the bend's radius) broke down into three rotating cells, one at the centre and one at each bank. The two cells near the banks rotated in the same direction as the bend-induced secondary flow circulation cell, whereas the central cell rotated in the opposite direction. The central cell downstream of the weir gradually disappeared as the other two cells merged and restored the bend-induced secondary flow cell. Kang et al. (2020a, 2020b) found similar secondary flows downstream of the rock vane, J-hook vane, bendway weir, cross vane, and w-weir, with a number of cells equal to the number of arms of the structures.

Decreasing the flow depth ($h = 0.5H$) led to recirculation flow downstream of the BAV near the water surface, where the longitudinal velocity was negative (Figure 8). This recirculation flow was caused by flow separation from the vane and continued up to the 76° section (equivalent to a distance $1.046L_v$ from the vane position). Recirculation zones can lead to the deposition of suspended sediments downstream of the vane. In addition, the recirculation zones are exposed to low hydraulic stress and less harsh hydraulic conditions, so they are valuable aquatic habitats for aquatic animals (Garcia et al., 2012). As shown in Figure 8, longitudinal velocities have their lowest value close to the bed (72–76° bend sections) but are not negative. Negative longitudinal velocities and recirculation flow do appear at the 68 and 70° sections (and between the BAV and the outer bank). In simulations with $h/H = 1$, 1.5 and 2, recirculation occurred neither upstream nor downstream of the BAV. Only an emerged BAV generates recirculation.

Recirculation flow is also formed behind some in-stream structures, but the dimensions depend in general on the structure's geometry and submergence. Kuhnle et al. (2008) reported that the recirculation length (or reattachment length) behind a vertically submerged trapezoidal spur dike was 1.6 times the length of the spur dike. Bahrami-Yarahmadi et al. (2020a) reported that a flow with negative longitudinal velocity exists downstream of vertical rectangular and triangular spur dikes in a straight flume up to a distance of 10.4 and 3 times the dike length, respectively. Kang et al. (2020a) observed that the size of a recirculation zone downstream of a bendway weir increased as the angle of the bendway weir increased. At the rock vane and J-hook vane, the recirculation zone was observed to be very small. Kang et al. (2020b) reported two small recirculation zones near the side walls downstream of a w-weir structure and near the water surface but did not observe these zones near the bed.

Figure 9 shows the flow pattern and longitudinal velocity contours at the 72° section (as an example) in different simulations, where 0 on the horizontal axis represents the inner bend wall, and 70 represents the outer bend wall. As the flow depth increases, flow velocity increases with increasing discharge at a constant Froude number. Therefore, the flow velocity is the highest in the simulation with a flow depth of $2H$. Moreover, Figure 9 shows that the flow velocity decreases near the outer bank following the installation of the BAV in all simulations, but to different extents. The most notable reduction in flow velocity near the outer bank corresponds to the simulation with a flow depth of $0.5H$. In this simulation, the deceleration zone is about 10 cm wide (equivalent to $0.476L_v$ or $0.142B$) at the 72° section and extends from the flume bed to the water surface. The deceleration zone becomes narrower with increasing flow depth. Moreover, when the flow depth exceeds the vane height (simulations with $h = 1.5H$ and $2H$), the vane fails to reduce the velocity of the uppermost layers of the stream (above 13 cm). In other words, layers above the 13-cm height are not affected by the vane. Therefore, submerging the vane and increasing the flow depth undermines the vane's effectiveness in slowing the flow down near the outer bank. The results showed that in all simulations with the BAV, the flow velocity near the outer bank further reduced at the 72° section than at other sections, but the velocity reduction was smaller at larger distances from the vane toward the end of the bend.

Figure 9 shows a vane-induced counter-clockwise vortex near the outer bank in all simulations, but its core position, appearance, and extent of development in the downstream direction differ in different simulations. With increasing flow depth, the core of the vane-induced vortex maintains its position relative to the outer bank but moves away from the water surface. Moreover, the vortex shape changes and becomes wider as the depth of flow increases. For example, in simulations with $h = 1H$ and $2H$, the vortex measured 14 and 20 cm in width (equal to $0.67L_v$ and $0.95\ L_v$) at the 76° section while measuring 22 and 40 cm (equal to $1.047L_v$ and $1.9L_v$) 2 m downstream the bend.

The downstream development of the vane-induced vortex in the simulation with a $0.5H$ flow depth differed

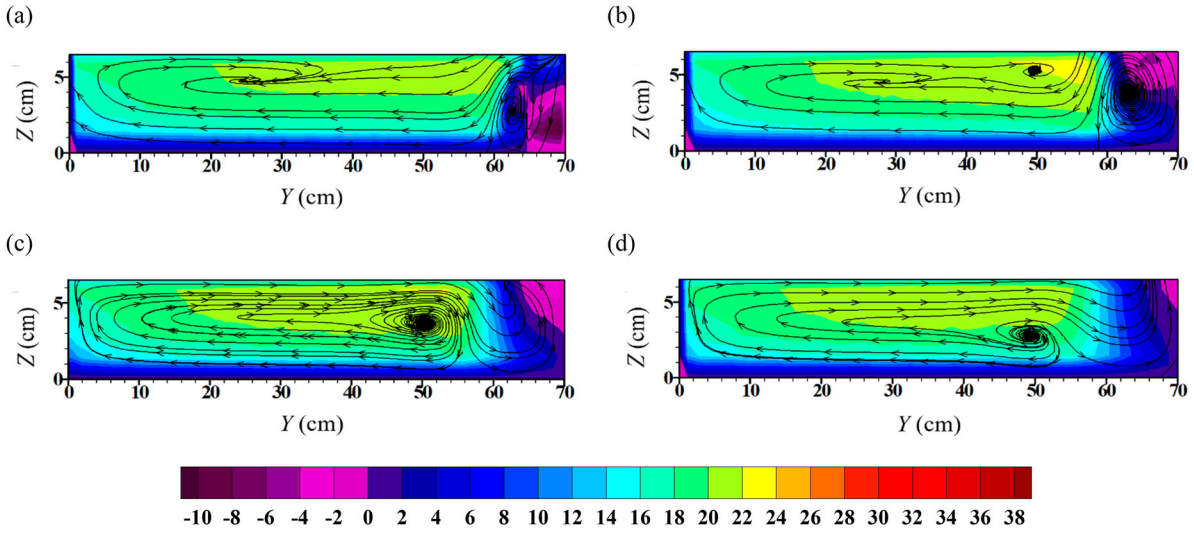

Figure 8. Flow pattern and longitudinal velocity contour (cm s^{-1}) for the simulation with 0.5*H* flow depth at sections: (a) 70°, (b) 72°, (c) 74°, (d) 76°.

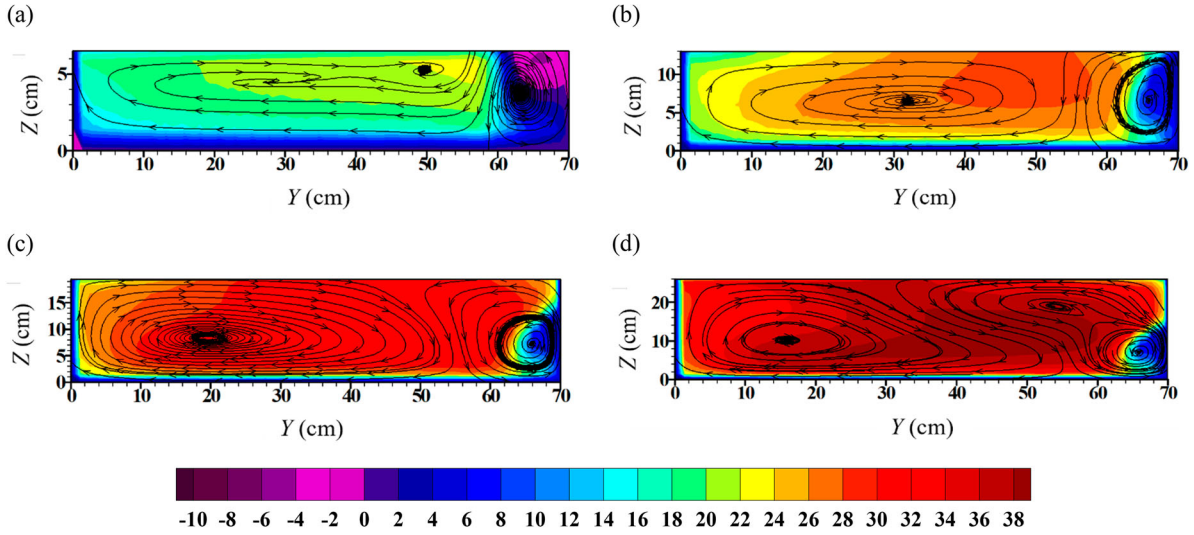

Figure 9. Flow pattern and longitudinal velocity contour (cm s^{-1}) at the 72° section for different flow depths: (a) 0.5*H*, (b) 1*H*, (c) 1.5*H*, (d) 2*H*.

from the submerged cases. The vane-induced vortex formed between the 70° and 74° sections (equivalent to $1.046L_v$) but disappeared further downstream. In simulations with $h/H = 1$, 1.5 and 2, the vane-induced vortex formed at the 70° section and extended 4 m downstream of the bend. As the straight reach downstream of the bend was only 4 m long, we do not know how far the vortex would have extended downstream in a longer reach.

According to Figure 9d, only in the simulation with $h = 2H$, the vane-induced vortex had two cores. In this simulation, the vane-induced vortex had only a single core between the 85° section and 50 cm downstream of the bend (Figure 10). According to Figure 10, three vortices appear between 1 and 4 m downstream of the bend in the simulation with the 2*H* flow depth. A clockwise vortex is caused by the bend, and the other two (one clockwise and one counter-clockwise) were generated by the BAV, close to the outer bank. The clockwise vortex close to the bed and the toe of the outer bank could scour the toe of the outer bank and transport sediment away from the outer bank to the centre of the waterway.

3.2. Bed shear stress

We calculated bed shear stress along the bend following Molls and Chaudhry (1995):

$$\tau_{b\theta} = \frac{\rho g}{c^2}\bar{V}_\theta\sqrt{\bar{V}_\theta^2 + \bar{V}_r^2} \tag{9}$$

$$\tau_{br} = \frac{\rho g}{c^2}\bar{V}_r\sqrt{\bar{V}_\theta^2 + \bar{V}_r^2} \tag{10}$$

$$\tau_b = \sqrt{\tau_{b\theta}^2 + \tau_{br}^2} \tag{11}$$

where τ_b denotes the bed shear stress, $\tau_{b\theta}$ and τ_{br} are bed shear stresses in the longitudinal and radial

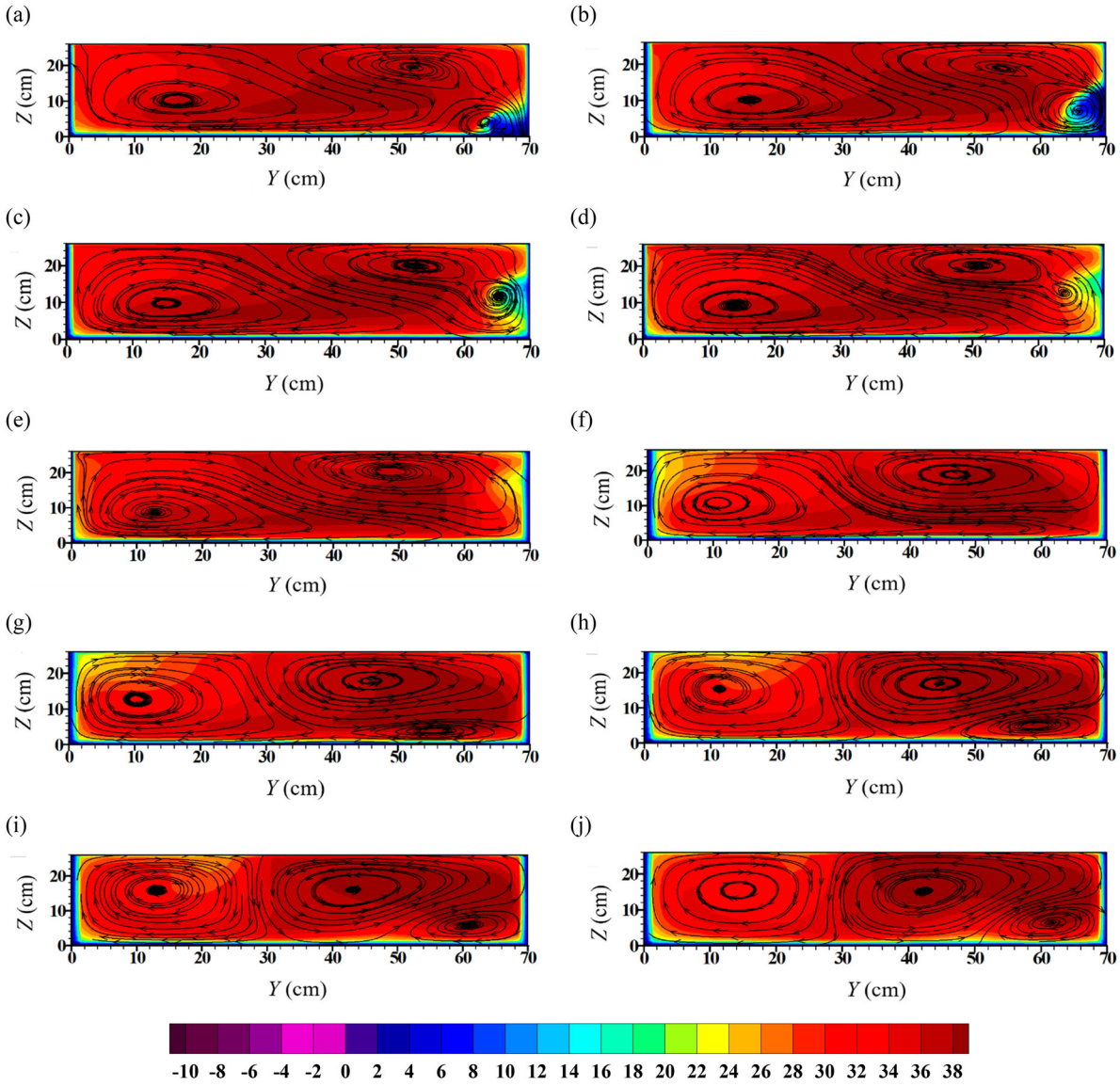

Figure 10. Flow pattern and longitudinal velocity contour (cm s^{-1}) for the simulation with a flow depth of 2*H* at sections: (a) 70°, (b) 72°, (c) 76°, (d) 80°, (e) 85°, (f) 0.5 m downstream the bend, (g) 1 m downstream the bend, (h) 2 m downstream the bend, (i) 3 m downstream the bend, (j) 4 m downstream the bend.

directions, $\bar{V}_\theta$ and $\bar{V}_r$ are the depth-averaged longitudinal and radial velocities, ρ denotes the fluid density ($\rho = 1000\,\mathrm{kg\,m^{-3}}$), g is the gravitational acceleration ($g = 9.81\,\mathrm{m\,s^{-2}}$), and c denotes the Chézy coefficient.

$$c = \frac{1}{n} R_h^{\frac{1}{6}} \tag{12}$$

where n is Manning's roughness coefficient, and R_h denotes the hydraulic radius.

From a hydraulics point of view, bed shear stresses larger than the incipient motion threshold cause erosion at the outer bank of the river bend. Accordingly, the performance of flow-altering structures in controlling erosion at the outer banks of bends must be evaluated in terms of the resulting bed shear stress reduction close to the outer bank and the maximum shear stress deviation toward the centre of the flume.

Figure 11 depicts the distribution of bed shear stress along the channel width at different sections in the simulation with a flow depth of 1*H*, where 0 on the horizontal axis represents the inner bend wall, and 70 represents the outer bend wall. As shown, in simulations without BAV, the maximum bed shear stress moves closer to the outer bank toward the end of the bend, naturally causing erosion in that area. Establishing the vane at the outer bend reduced bed shear stress on the outer bank and moved the maximum bed shear stress away from the bank toward the centre of the flume. This function of the BAV can protect the outer bank from erosion. The most notable shear stress reduction was observed between the 72° and 80° sections. The BAV was less effective in reducing the bed shear stress downstream the 80° section than upstream. The effect of the vane decreased further away from its position.

Figure 12 shows the transverse distribution of bed shear stress at the 74° section (as an example) in different simulations. Installing the BAV in the outer bend reduced the bed shear stress in that area. However, the extent of reduction varied in different simulations. In

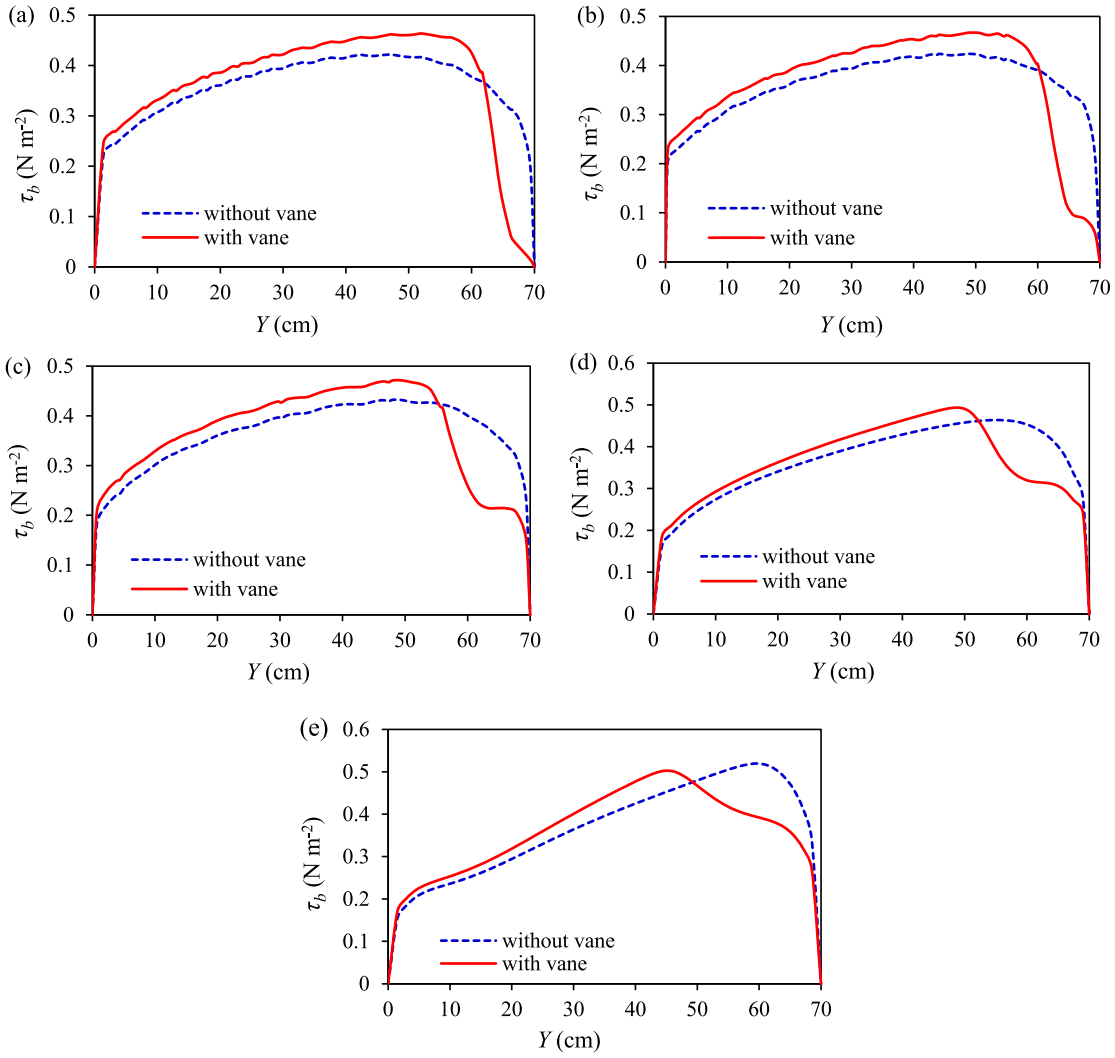

Figure 11. Transverse distribution of bed shear stress for the simulation with a 1*H* flow depth at different sections: (a) 72°, (b) 74°, (c) 80°, (d) 90°, (e) 2 m downstream the bend.

the case of the simulation with a 0.5*H* flow depth, the BAV managed to suppress nearly 100% of the bed shear stress at the outer bank, bringing it virtually down to zero. Increasing the flow depth undermined the BAV's effects on the bed shear stress reduction. According to the results, the reduction of bed shear stress at the 74° section reached a maximum of 73, 68 and 60% in the simulations with $h = 1H$, $1.5H$, and $2H$, respectively.

Moreover, Figure 12 shows that the bed shear stress increased in simulations without the BAV due to the constant Froude number but higher flow velocity.

Table 2 presents the details of bed shear stress reduction (average and maximum reduction) near the outer bank in different simulations with the BAV. The effects of the BAV on the bed shear stress reduction were found to extend to sections upstream of the vane and downstream of the bend. In the simulation with the 0.5*H* flow depth, the bed shear stress decreased less than 10% upstream of the 65° section. In simulations with $h = 1H$, $1.5H$ and $2H$, the bed shear stress decreased less than 10% upstream of the 68° section. Upstream of the BAV, the maximum reduction of bed shear stress in simulations with $h = 0.5H$, $1H$, $1.5H$ and $2H$ was found to be 100, 75, 54 and 43%, respectively, which occurred at the 70° section.

Table 2 also shows that the BAV was more effective in reducing the bed shear stress downstream of the vane than upstream. Moreover, the BAV reduced the bed shear stress more effectively in simulations with $h = 0.5H$ and $1H$ than in those with $h = 1.5H$ and $2H$. An increased flow depth undermines the BAV's effectiveness in reducing the bed shear stress around the outer bank and, consequently, its capacity to protect the outer bank against erosion.

The bed shear stress was reduced most at the 72° section, where the vane was positioned. Here the bed shear stress reduction reached a maximum of 100, 93, 80 and 73% in the simulations with $h = 0.5H$, $1H$, $1.5H$ and $2H$, respectively. Studying a single, 30-cm long BAV with the same height as the flow depth (13 cm), Bahrami-Yarahmadi et al. (2020b) reported bed shear stress reduction near the outer bank upstream of the structure to reach a maximum of 67% at the 70° section. They also reported that the maximum reduction of bed shear stress at the 72° section is equal to 80%.

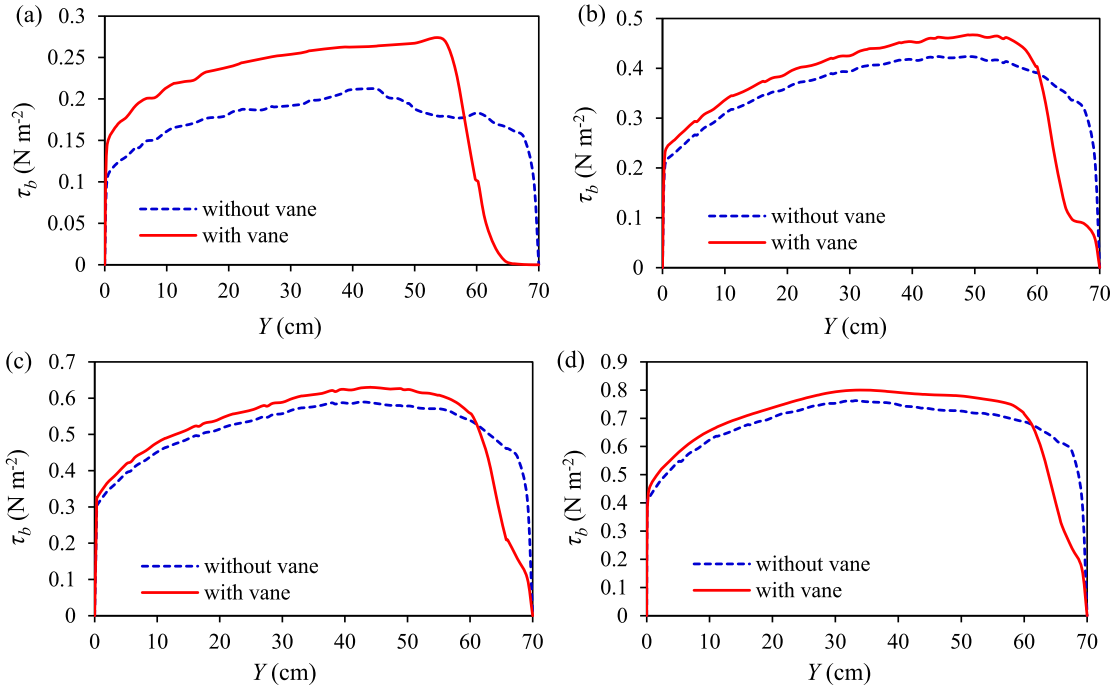

Figure 12. Transverse distribution of bed shear stress at the 74° section for different flow depths: (a) 0.5*H*, (b) 1*H*, (c) 1.5*H*, (d) 2*H*.

Table 2. Bed shear stress reduction close to the outer bank for simulations with the BAV.

	h = 6.5 cm		h = 13 cm		h = 19.5 cm		h = 26 cm	
Cross sections (°)	Average reduction (%)	Maximum reduction (%)	Average reduction (%)	Maximum reduction (%)	Average reduction (%)	Maximum reduction (%)	Average reduction (%)	Maximum reduction (%)
60	4	8	3	4	2	3	1	2
65	13	23	4	10	3	5	2	4
68	38	74	12	31	8	22	8	18
70	75	100	45	75	29	54	26	43
72	79	100	54	93	44	80	37	73
74	68	100	51	73	36	68	31	60
80	52	93	27	43	26	43	24	43
90	32	57	19	29	15	24	14	27
90° + 1 m	23	46	18	25	10	16	8	14
90° + 2 m	15	37	17	24	8	12	4	10

Figure 13 shows the position of the maximum bed shear stress along the bend in different simulations. In simulations without a BAV, the maximum bed shear stress occurs close to the inner bank at the beginning of the bend, gradually moving toward the centre of the flume further into the bend and eventually toward the outer bank close to the end of the bend. The maximum bed shear stress occurs near the outer bank downstream of the bend. This relocation of the maximum causes erosion at the outer bank of the bend. Accordingly, flow-altering structures used to control erosion on the outer banks of bends must be able to reduce bed shear stress at the outer bank and deviate the maximum bed shear stress from the outer bank toward the centre of the waterway. As shown in Figure 13, the BAV successfully pushed the maximum bed shear stress away from the outer bank in all cases. The BAV performed notably better in simulations with $h = 1H$ and 1.5*H*, whereas the poorest performance was observed in the simulation with $h = 2H$ where the BAV failed to move the maximum bed shear stress further away from the outer bank (as much as other simulations). It did reduce the bed shear stress close to the outer bank, albeit to a lesser extent than in other simulations (Table 2). In the simulation with a 1*H* flow depth, the maximum bed shear stress at the 80° section, 85° section, 90° section, 1 m downstream the bend, and 2 m downstream the bend occurred at points where $y/B = 0.292, 0.257, 0.207, 0.15$ and 0.15, respectively (y: distance from the outer bank, B: flume width) without the vane and at points where $y/B = 0.314, 0.314, 0.314, 0.32$ and 0.362, respectively, with the vane.

Other in-stream structures also move high-shear stress zones away from the outer bank, but their impact depends on their geometry, angle, number and position within the bend. Khosronejad, Diplas et al. (2016), Khosronejad, Kozarek, Diplas et al. (2018) found that the installation of a rock vane or a 50° bendway weir at the apex of the river bend deflected the high-shear stress zone from the outer bank. However, a structure was not enough to protect the entire outer bank.

Scour at the nose of flow-altering structures and the development of the scour hole in width and depth destroy these structures. The key factor in scouring the

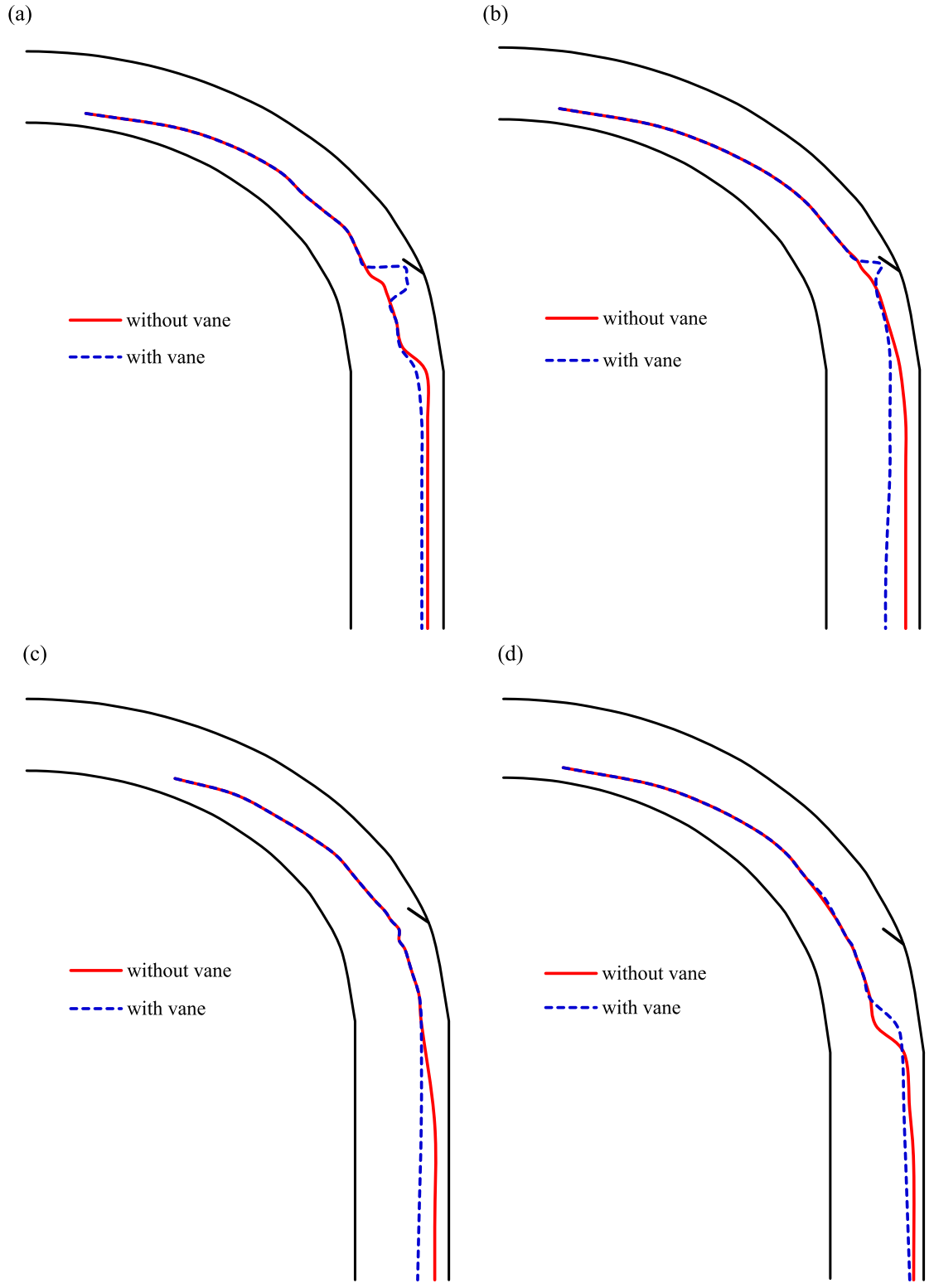

Figure 13. The position of the maximum bed shear stress along the bend in simulations with different flow depths: (a) 0.5*H*, (b) 1*H*, (c) 1.5*H*, (d) 2*H*.

noses of flow-altering structures in laboratory experiments is that the bed shear stress exceeds the critical shear stress for sediment motion (clear-water scour), but this is not necessarily the case in rivers (live-bed scour). It was demonstrated that the bed shear stress reaches 0.25, 0.45, 0.6 and 0.76 N m^{-2} (equal to 1.67, 1.45, 1.3 and 1.24 times the average bed shear stress upstream of the bend) around the BAV nose in simulations with $h = 0.5H$, $1H$, $1.5H$ and $2H$, respectively. Increasing the flow depth (through a constant Froude number and increased flow velocity) increased bed shear stress at the structure's nose, making scour more likely to occur in this area. Kang et al. (2020a) reported a high-bed-shear-stress zone formed downstream of the tip of the rock vane and several high-bed-shear-stress zones were formed downstream of the

boulders at the tip of the J-hook vane. Moreover, high shear stress zones were observed downstream of the 60° and 80° bendway weirs, but their distance from the side wall was greater compared to the rock vane and J-hook vane. The bed shear stress distribution was completely similar to the rock vane downstream of the cross vane and w-weir structures. In these two structures, high-shear stress zones were observed downstream of the arms.

4. Conclusions

The novel BAV is designed at bankfull discharge (the BAV's height is equal to flow depth) and attached to the bank at a slight angle to the upstream bank. The BAV keeps the main flow away from the bank: generating a vortex that counteracts with river bend-induced vortex which results in the reduction of the banks' toe scour. Since the performance of the BAV for higher and lower flow depth is uncertain, we validated the numerical model of Flow3D to study the flow pattern and bed shear stress around a single BAV in a 90° mild bend under submerged (three submergence levels) and emerged conditions. Simulations were executed for configurations with and without a BAV and flow depths of 0.5, 1, 1.5 and 2 times the BAV height. The final results demonstrated that:

I. The BAV created a vortex near the outer bank, rotating opposite to the bend-induced vortex in both submerged and emerged conditions.
II. Increasing the flow depth altered the shape of the vane-induced vortex. Unlike in other simulations, the vane-induced vortex had two cores in the simulation with a $2H$ flow depth and transformed into two opposing vortices downstream of the bend.
III. A deeper flow expanded the width of the vane-induced vortex. For example, in simulations with $h = 1H$ and $2H$, the vortex width was $0.67L_v$ and $0.95L_v$ at the 76° section.
IV. In all simulations, a vane-induced vortex formed at the 70° section, but the extent of its downstream development differed in the simulation with a $0.5H$ flow depth. The vortex extended up to the 74° section (equal to $1.046L_v$) in the simulation with a $0.5H$ flow depth, despite continuing up to 4 m downstream the bend for flow depths of $1H$, $1.5H$ and $2H$.
V. A recirculation flow with a length of $1.046L_v$ developed behind the BAV in the emerged condition. Similar flow conditions were not observed in the submerged vane.
VI. The BAV reduced the flow velocity close to the outer bank, but the extent of this reduction depended on the flow depth. The smallest and largest reduction corresponded to $2H$ and $0.5H$ flow depths, respectively. In simulations where the flow depth exceeded the vane height ($1.5H$ and $2H$), the BAV failed to slow down the fluid in layers above the 13-cm height.
VII. The BAV gradually reduced bed shear stress near the outer bank upstream and downstream of the vane. The bed shear stress was reduced the most at the vane position (the 72° section). Bed shear stress reduction decreased further away from the vane. Changing the flow depth affected the vane's performance in reducing shear stress, as bed shear stress was reduced more in cases where the flow depth was $0.5H$ and $1H$ than in those where it was $1.5H$ or $2H$.
VIII. The BAV successfully pushed the maximum bed shear stress away from the outer bank under submerged and emerged conditions. The vane performed better in simulations with $h = 1H$ and $1.5H$, whereas the worst performance was observed in the simulation with a $2H$ depth of flow.

Based on these results, we conclude that the BAV must be higher than or as high as the flow depth for bankfull discharge to control bank erosion on bends.

Disclosure statement

No potential conflict of interest was reported by the author(s).

Funding

We are grateful to the Research Council of Shahid Chamran University of Ahvaz for financial support [SCU.WH99.31373].

Notation

A_x, A_y, A_z	fractional area of flow in the x, y, z directions (m^2)
B	flume width (m)
c	Chézy coefficient ($m^{\frac{1}{2}}s^{-1}$)
d_{16}	grain size for which 16% of sampled particles are finer (m)
d_{50}	median diameter of sediment particles (m)
d_{84}	grain sizes for which 84% of sampled particles are finer (m)
$\mathsf{F_r}$	Froude number (–)
f_x, f_y, f_z	accelerations caused by viscosity in the x, y, z directions ($m\ s^{-2}$)
g	gravitational acceleration ($m\ s^{-2}$)
G_x, G_y, G_z	body accelerations ($m\ s^{-2}$)
h	flow depth (m)
H	height of the bank-attached vane (m)
k	turbulence kinetic energy ($m^2\ s^{-2}$)
L	effective length of the bank-attached vane (m)
L_v	length of the bank-attached vane (m)

n	Manning's roughness coefficient (–)
O_i	observed velocities (m s^{-1})
R	average bend radius (m)
Re	Reynolds number (–)
R_h	hydraulic radius (m)
R_{SOR}	mass source (kg m^{-3})
S_i	simulated velocities from Flow3D (m s^{-1})
T	time (s)
u_i	velocities in the x, y, z directions (m s^{-1})
u_*	shear velocity (m s^{-1})
V_f	fractional volume of flow (m^3)
$\bar{V}_r$	depth-averaged radial velocity (m s^{-1})
$\bar{V}_\theta$	depth-averaged longitudinal velocity (m s^{-1})
Y	distance from the outer bank (m)
y_s	distance from the wall to the centre of the first cell (m)
y^+	dimensionless wall distance (–)
α	angle of bank-attached vane with the upstream bank (°)
ε	turbulence dissipation rate (m^2 s^{-3})
μ	molecular viscosity (N s m^{-2})
μ_t	turbulent viscosity (N s m^{-2})
ν	kinematic viscosity of the fluid (m^2 s^{-1})
ρ	mass density of the fluid (kg m^{-3})
σ_g	geometric standard deviation (–)
τ_b	bed shear stress (N m^{-2})
$\tau_{b\theta}$	bed shear stress in the longitudinal direction (N m^{-2})
τ_{br}	bed shear stress in the radial direction (N m^{-2})

References

Bahrami Yarahmadi, M., & Shafai Bejestan, M. (2016a). Sediment management and flow patterns at river bend due to triangular vanes attached to the bank. *Journal of Hydro-environment Research*, *10*, 64–75. https://doi.org/10.1016/j.jher.2015.10.002

Bahrami Yarahmadi, M., & Shafai Bejestan, M. (2016b). Comparison of erosion and sedimentation patterns facilitated by a spur dike and a triangular-shaped vane structures in a 90° mild bend under the influence of different Froude numbers. *Water Resources Engineering*, *8*(27), 31–42.

Bahrami-Yarahmadi, M. (2014). *Experimental study of the combined bank attached-vane and footing on bed topography variations in a 90° bend* [PhD thesis]. Faculty of Water and Environmental Engineering, Shahid Chamran University of Ahvaz, Iran (in Persian). https://ganj.irandoc.ac.ir/#/articles/103aadff53b9df58cdb0d43ab017cf4b

Bahrami-Yarahmadi, M., Pagliara, S., Yabarehpour, E., & Najafi, N. (2020a). Study of scour and flow patterns around triangular-shaped spur dikes. *KSCE Journal of Civil Engineering*, *24*(11), 3279–3288. https://doi.org/10.1007/s12205-020-2261-x

Bahrami-Yarahmadi, M., Shafai-Bejestan, M., & Pagliara, S. (2020b). An experimental study on the secondary flows and bed shear stress at a 90-degree mild bend with and without triangular vanes. *Journal of Hydro-environment Research*, *33*, 1–9. https://doi.org/10.1016/j.jher.2020.10.001

Bhuiyan, F., Hey, R. D., & Wormleaton, P. R. (2010). Bank-attached vanes for bank erosion control and restoration of river meanders. *Journal of Hydraulic Engineering*, *136*(9), 583–596. https://doi.org/10.1061/(ASCE)HY.1943-7900.0000217

Biedenharn, D. S., Elliott, C. M., & Watson, C. C. (1997). *The WES stream investigation and streambank stabilization handbook*. U.S. Army Engineer, Waterways Experiment Station (WES).

Blanckaert, K., & Graf, W. H. (2001). Mean flow and turbulence in open channel bend. *Journal of Hydraulic Engineering*, *127*(10), 835–846. https://doi.org/10.1061/(ASCE)0733-9429(2001)127:10(835)

Bora, K., & Kalita, H. M. (2021). Best groyne series as countermeasure against river bend scour. *Water Management*, *174*(4), 198–211.

Bracmort, K. S., Arabi, M., Frankenberger, J. R., Engel, B. A., & Arnold, J. G. (2006). Modeling long-term water quality impact of structural BMPs. *American Society of Agricultural and Biological Engineers*, *49*(2), 367–374.

Deng, S. S., Xia, J. Q., Zhou, M. R., & Lin, F. F. (2019). Coupled modeling of bed deformation and bank erosion in the Jingjiang Reach of the middle Yangtze River. *Journal of Hydrology*, *568*, 221–233. https://doi.org/10.1016/j.jhydrol.2018.10.065

Fathi-Moghaddam, M., Tavakol Sadrabadi, M., & Rahmanshahi, M. (2018). Numerical simulation of the hydraulic performance of triangular and trapezoidal gabion weirs in free flow condition. *Flow Measurement and Instrumentation*, *62*, 93–104. https://doi.org/10.1016/j.flowmeasinst.2018.05.005

Ferro, V., Shokrian-Hajibehzad, M., Shafai-Bejestan, M., & Kashefipour, S. M. (2019). Scour around a permeable groin combined with a triangular vane in river bends. *Journal of Irrigation and Drainage Engineering*, *145*(3), 04019003. https://doi.org/10.1061/(ASCE)IR.1943-4774.0001380

Galia, T., Škarpich, V., Hradecký, J., & Přibyla, Z. (2016). Effect of grade-control structures at various stages of their destruction on bed sediments and local channel parameters. *Geomorphology*, *253*, 305–317. https://doi.org/10.1016/j.geomorph.2015.10.033

Garcia, X.-F., Schnauder, I., & Pusch, M. T. (2012). Complex hydromorphology of meanders can support benthic invertebrate diversity in rivers. *Hydrobiologia*, *685*(1), 49–68. https://doi.org/10.1007/s10750-011-0905-z

Gupta, H. V., Sorooshian, S., & Yapo, P. O. (2001). Status of automatic calibration for hydrologic models: Comparison with multilevel expert calibration. *Journal of Hydrologic Engineering*, *4*(2), 135–143. https://doi.org/10.1061/(ASCE)1084-0699(1999)4:2(135)

Hey, R. D. (1996). *Environmentally sensitive river engineering*. River restoration, G. Petts & P. Calow (Eds.) (pp. 80–105). Blackwell Science.

Jalili, M., Bakhtiyari, M., Kashfipour, S. M., & Shehni Karam Zadeh, N. (2018). Experimental analysis of the effect of bandal-like spur dike submergence on bed topography in 90 degree bend. *Irrigation Sciences and Engineering*, *40*(4), 141–154.

Jia, Y., Scott, S., Xu, Y., Huang, S., & Wang, S. S. Y. (2005). Three-dimensional numerical simulation and analysis of flows around a submerged weir in a channel bendway. *Journal of Hydraulic Engineering*, *131*(8), 682–693. https://doi.org/10.1061/(ASCE)0733-9429(2005)131:8(682)

Julien, P. Y. (2002). *River mechanics* (p. 434). Cambridge University Press.

Kalamizadeh, M. R., Kamanbedast, A. M., Shafai-Bejestan, M., Masjedi, A., & Hasonizadeh, H. (2021). Laboratory evaluation of permeable triangular vanes with six-pillar elements placed in the outer bend of a 180° flume. *Arabian Journal of Geosciences*, *14*(4), 235. https://doi.org/10.1007/s12517-021-06498-5

Kang, S., Khosronejad, A., Hill, C., & Sotiropoulos, F. (2020a). Mean flow and turbulence characteristics around single-arm instream structures. *Journal of Hydraulic Research*, *59*(3), 404–419. https://doi.org/10.1080/00221686.2020.1780494

Kang, S., Khosronejad, A., Hill, C., & Sotiropoulos, F. (2020b). Mean flow and turbulence characteristics around multiple-arm instream structures and comparison with single-arm structures. *Journal of Hydraulic Engineering*, *146*(5), 04020030. https://doi.org/10.1061/(ASCE)HY.1943-7900.0001738

Kashyap, S., Constantinescu, G., Rennie, C., Post, G., & Townsend, R. (2012). Influence of channel aspect ratio and curvature on flow, secondary circulation, and bed shear stress in a rectangular channel bend. *Journal of Hydraulic Engineering*, *138*(12), 1045–1059. https://doi.org/10.1061/(ASCE)HY.1943-7900.0000643

Khosronejad, A., Diplas, P., & Sotiropoulos, F. (2016). Simulation-based optimization of in-stream structures design: bendway weirs. *Journal of Environmental Fluid Mechanics*, *17*(1), 79–109. https://doi.org/10.1007/s10652-016-9452-5

Khosronejad, A., Hill, C., Kang, S., & Sotiropoulos, F. (2013). Computational and experimental investigation of scour past laboratory models of stream restoration rock structures. *Advances in Water Resources*, *54*, 191–207. https://doi.org/10.1016/j.advwatres.2013.01.008

Khosronejad, A., Kozarek, J. L., Diplas, P., & Sotiropoulos, F. (2015). Simulation-based optimization of in-stream structures design: J-hook vanes. *Journal of Hydraulic Research*, *53*(5), 588–608. https://doi.org/10.1080/00221686.2015.1093037

Khosronejad, A., Kozarek, J. L., & Sotiropoulos, F. (2014). Simulation-based approach for stream restoration structure design: Model development and validation. *Journal of Hydraulic Engineering*, *140*(9), 04014042. https://doi.org/10.1061/(ASCE)HY.1943-7900.0000904

Khosronejad, A., Kozarek, L. J., Diplas, P., Hill, C., Jha, R., Chatanantavet, P., Heydari, N., & Sotiropoulos, F. (2018). Simulation-based optimization of in-stream structure design: Rock-vanes. *Environmental Fluid Mechanics*, *18*(3), 695–738. https://doi.org/10.1007/s10652-018-9579-7

Koken, M., & Gogus, M. (2015). Effect of spur dike length on the horseshoe vortex system and the bed shear stress distribution. *Journal of Hydraulic Research*, *53*(2), 196–206. https://doi.org/10.1080/00221686.2014.967819

Kuhnle, R. A., Jia, Y., & Alonso, C. V. (2008). Measured and simulated flow near a submerged spur dike. *Journal of Hydraulic Engineering*, *134*(7), 916–924. https://doi.org/10.1061/(ASCE)0733-9429(2008)134:7(916)

Mastbergen, D. R., Beinssen, K., & Nédélec, Y. (2019). Watching the beach steadily disappearing: The evolution of understanding of retrogressive breach failures. *Journal of Marine Science and Engineering*, *7*(10), 368. https://doi.org/10.3390/jmse7100368

Molls, T., & Chaudhry, M. H. (1995). Depth-averaged open-channel flow model. *Journal of Hydraulic Engineering*, *121*(6), 453–465. https://doi.org/10.1061/(ASCE)0733-9429(1995)121:6(453)

NRCS. (2007). *Stream restoration design, NEH 654*. United States Department of Agriculture, National Resource Conservation Service.

Oberhagemann, K., Aminul Haque, A. M., & Thompson, A. (2020). A century of riverbank protection and river training in Bangladesh. *Water*, *12*(11), 3018. https://doi.org/10.3390/w12113018

Odgaard, A. J. (2009). *River training and sediment management with submerged vanes*. ASCE Press, ISBN 978-0-7844-0981-7.

Pagliara, S., & Kurdistani, S. M. (2017). Flume experiments on scour downstream of wood stream restoration structures. *Geomorphology*, *279*, 141–149. https://doi.org/10.1016/j.geomorph.2016.10.013

Pandey, M., Ahmad, Z., & Sharma, P. K. (2018). Scour around impermeable spur dikes: A review. *ISH Journal of Hydraulic Engineering*, *24*(1), 25–44. https://doi.org/10.1080/09715010.2017.1342571

Parsaie, A., Shareef, S. J. S., Haghiabi, A. H., Irzooki, R. H., & Khalaf, R. M. (2022). Numerical simulation of flow on circular crested stepped spillway. *Applied Water Science*, *12*(9), 1–10. https://doi.org/10.1007/s13201-022-01737-w

Rodi, W. (2017). *Turbulence models and their application in hydraulics: A state-of-the-art review* (3st ed.). CRC Press LLC. https://doi.org/10.1201/9780203734896

Rodríguez-Amaya, C., Durán-Ariza, A., & Duarte-Méndez, S. (2020). Submerged vane technology in Colombia: Five representative projects. *Water*, *12*(4), 984. https://doi.org/10.3390/w12040984

Rosgen, D. L. (1996). *Applied river morphology*. Wildland Hydrology, Pagosa Spring, Colo.

Rosgen, D. L. (2006). *The cross-vane, w-weir, and j-hook structures: Description, design and application for stream stabilization and river restoration*. Wildland Hydrology, Inc.

Safaripour, N., Vaghefi, M., & Mahmoudi, A. (2022). Experimental study of the effect of submergence ratio of double submerged vanes on topography alterations and temporal evaluation of the maximum scour in a 180-degree bend with a bridge pier group. *International Journal of River Basin Management*, *20*(4), 1–34. https://doi.org/10.1080/15715124.2020.1837144

Salehzadeh, M., Hemmati, M., Yasi, M., & Lanzoni, S. (2023). Effects of relative curvature radius on erosion and sedimentation patterns in a 90° bend with and without bendway weirs. *Journal of Hydraulic Research*, *61*(5), 796–802. https://doi.org/10.1080/00221686.2023.2242813

Santhi, C., Arnold, J. G., Williams, J. R., Dugas, W. A., Srinivasan, R., & Hauck, L. M. (2002). Validation of the SWAT model on a large river basin with point and nonpoint sources. *Journal of the American Water Resources Association*, *37*(5), 1169–1188. https://doi.org/10.1111/j.1752-1688.2001.tb03630.x

Shampa, S., Hasegawa, Y., Nakagawa, H., Takebayashi, H., & Kawaike, K. (2020). Three-dimensional flow characteristics in slit-type permeable spur dike fields: Efficacy in riverbank protection. *Water*, *12*(4), 964. https://doi.org/10.3390/w12040964

Shields, F. D. (1983). Design of habitat structures for open channels. *Journal of Water Resources Planning and Management*, *109*(4), 331–344. https://doi.org/10.1061/(ASCE)0733-9496(1983)109:4(331)

Shokrian Hajibehzad, M., Shafai Bejestan, M., & Ferro, V. (2020). Investigating the performance of enhanced permeable groins in series. *Water*, *12*(12), 3531. https://doi.org/10.3390/w12123531

Van der Wal, M. (2020). Bank protection structures along the Brahmaputra-Jamuna River; A study of flow slides. *Water*, *12*(9), 2588. https://doi.org/10.3390/w12092588

Yakhot, V., Thangam, S., Gatski, T. B., Orszag, S. A., & Speziale, C. G. (1992). Development of turbulence models for shear flows by a double expansion technique. *Physics of Fluids A Fluid Dynamics*, *4*(7), 1510–1520. https://doi.org/10.1063/1.858424

Zhang, H., Nakagawa, H., Kawaike, K., & Baba, Y. (2009). Experiment and simulation of turbulent flow in local scour around a spur dyke. *International Journal of Sediment Research*, *24*(1), 33–45. https://doi.org/10.1016/S1001-6279(09)60014-7